Journal of Molecular Structure 1216 (2020) 128295

Contents lists available at ScienceDirect

Journal of Molecular Structure

journal homepage: http://www.elsevier.com/locate/molstruc

Experimental and theoretical charge density analysis of skin whitening agent kojic acid

Asma Hasil [a], Arshad Mehmood [b], Sajida Noureen [a], Maqsood Ahmed [a, *]

[a] Materials Chemistry Laboratory, Department of Chemistry, The Islamia University of Bahawalpur, 63100, Bahawalpur, Pakistan
[b] Department of Chemistry & Biochemistry, Texas Christian University, Fort Worth, Texas, 76129, USA

ARTICLE INFO

Article history:
Received 31 January 2020
Received in revised form
7 April 2020
Accepted 17 April 2020
Available online 23 April 2020

ABSTRACT

The charge density analysis from high resolution X-ray diffraction at 100 K was carried out to understand the structure properties relationship and binding fashion in anti-Tyrosinase Kojic acid. The experimental results were validated from periodic theoretical calculations using B3LYP/6−311++g(2 d, 2p) level of theory. The experimental electron density and Laplacian of electron density was calculated and compared from theoretical displaying the distribution of respective charges in the crystal field of Kojic acid molecule. An analysis of the electrostatic potential surface provides insight into anti-melanogenesis function.

1. Introduction

Cosmetic industry has been continuously using new biologically active ingredients for several decades to fulfill the market demands. The consumption of skin whitening agents and skin care products is an industry worth billions of dollars globally. In the cosmetic industry, whitening agents [1] have maintained a high consumption since the late 1980. The global market for skin whitening agents is always found of using clinically safe and effective cosmetic formulations. Melanogenesis is the process of melanin formation by the melanocytes in the skin and hair follicles [2]. This synthesized melanin plays crucial role to protect the skin from the harmful ultraviolet (UV) radiations but uneven excessive secretion of melanin causes different aesthetic problems like lentigo, freckles, age spots, melasma.

Melanin synthesis in humans is attributed to three enzymes Tyrosinase, Tyrosinase related protein I (Trp1) [3] and Tyrosinase related protein II (Trp2) [4]. Tyrosinase [5,6] is one of the three enzymes used in the biosynthesis of melanin and is the primary determinant of the human skin, certain structures of brain, hair color and iris color of the eye; the colours of which depends on the quantity of melanin distribution [7−9]. Tyrosinase is the critical rate-limiting enzyme located in the melanosomes where melanin is synthesized. Tyrosinase is the copper containing enzyme that catalyze the hydroxylation of tyrosine to 3,4-dihydroxyphenylalanine (DOPA) and oxidation of DOPA to dopaquinone. Dopaquinone is the reactive substance and spontaneously polymerizes to form melanin [10,11].

Kojic acid (KA) is one of the famous metabolites used as Tyrosinase inhibitor. Because of its inhibitory effect on Tyrosinase it has been widely used in the cosmetic industries as skin lightning/depigmenting agent. KA metabolite binds with the active site of Tyrosinase enzyme via chelation of copper thus inhibiting the Melanogenesis. The present research work is motivated by the fact that despite wide range usage in cosmetic industry and pharmaceutical applications, there is lack of systematic study of the plausible mechanism of binding with subsequent action, bonding characteristics and the electron charge density distributions. The KA structure is chemically interesting because of the presence of wide range of reaction centres with the presence of oxygen skeleton as well as several proton donor and acceptor sites. The presence of two OH groups in the KA molecule underlines its acidity which may also suggest its behaviour as a photo acid [12].

So, one way of understanding the unravelling hitherto explored aspects of depigmenting agent KA-Tyrosinase complex, their mechanism of action and finally the expression reaching the possibility of whitening or depigmenting the skin is by determining the charge density properties of Tyrosinase inhibitor, KA. Topological analysis and electrostatic properties derived from the electron density distribution has proven to be very useful [13−16] as the

* Corresponding author.
E-mail addresses: asmahasil@gmail.com (A. Hasil), arshad.mehmood@tcu.edu (A. Mehmood), sajida.noureen@iub.edu.pk (S. Noureen), maqsood.ahmed@iub.edu.pk (M. Ahmed).

https://doi.org/10.1016/j.molstruc.2020.128295
0022-2860/

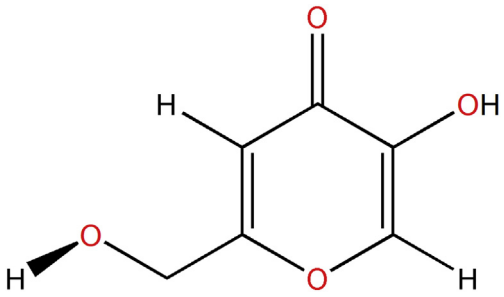

Scheme 1.

strength of the metabolite-receptor interactions depends on the electron density distributions mainly. Experimental electron density studies of various drug and biomolecules, such as estrone [17,18] genistein, olefin, aziridine, oxirane [13], paracetamol [15], 17α-estradiol $0.5H_2O$ [19], aspirin [20], ethionamide, pyrazinamide [21], isoniazid [22], 16α, 17β-estriol [23], 2-nitro-imidazole [24], Andrographolide [25], Hippuric Acid [26] and many others have been carried out and successfully established the importance of the electron density studies for understanding the chemical nature of a molecule. The electrostatic and structural complementarity of a drug molecule with receptor site amino acid residues is the foundation for the molecular recognition. The multipole model of experimental electron density adequately explains the directional effects of these polar interactions [27]. The electron density analysis helps in determination of the mode of action of a drug molecule by marking the reactive sites of the molecule [13,14]. The electron density analysis of KA will help to determine the behaviour of metabolite molecule to bind with active site of the biological environment of Tyrosinase enzyme as an Enzyme-substrate complex. Accurate determination of the electrostatic properties of the KA molecule from the experiment can reveal very valuable information about the Tyrosinase-inhibitory action and anti-melanin properties. This unravelling knowledge about the KA molecule can help to find a new route to particularly determine the binding of KA with the active site of Tyrosinase via chelation of copper cofactor resulting in the inhibition of melanin formation and finally its expression in the skin 'fairness'.

In the present study, the experimental electron density distribution of KA is determined from the high resolution X-ray diffraction data at the low temperature of 100 (1) K. The electron density, the Laplacian of electron density distribution and the electrostatic properties are calculated for KA. The topological analysis of strong and weak intermolecular interactions of the KA molecule in the crystal has also been carried out. The experimental results are compared with the corresponding theoretical solid-state quantum chemical calculations using density functional theory (DFT).(Scheme 1)

2. Experimental

2.1. Crystallization and data collection

The title compound (KA) was purchased from a commercial supplier and used without further purification. It was crystallized by the slow evaporation of a concentrated solution in a mixture of ethanol-methanol solvents in 1:1 stoichiometric ratio at room temperature. Brown-Prism shaped crystals were obtained after few days. A single crystal with dimensions $0.234 \times 0.290 \times 0.439$ mm^3 was used for diffraction experiment (Fig. S1). High resolution single crystal X-ray diffraction data were collected at 100 (1) K using Mo Kα radiation (λ = 0.71073 Å) from a microfocus source on Bruker D8 Venture diffractometer equipped with PHOTON II detector [28]. The crystal was mounted on a glass needle using vacuum grease and placed on four-circle goniometer head under a stream of compressed nitrogen using Oxford Cobra device to cool from room temperature to 100 K during the entire experiment. The Cobra device provided excellent temperature stability better than ±1 K during the entire experiment. Bragg intensities were collected using 1.0°ω and ϕ scan width. Two different exposure times of 10s and 20s per frame were used for low angle and high angle respectively resulting in a total of 54,643 reflections up to a $Sin\theta/\lambda_{max}$ of 1.125 (Å^{-1}). SAINT program was used for cell refinement and reduction of data [28]. A numerical absorption correction using the real face indices was carried out using SADABS program [29]. Table 1 lists all the crystallographic and refinement statistics.

2.2. Structure solution and IAM Olex2 refinement

The crystal structure was solved in monoclinic crystal system with space group $P2_1/n$ and refined by using Olex2 [30] Fig. 1. All the H atoms were clearly visible in the difference maps. However, a riding model [31] was used for the hydrogen atoms attached to carbon C_{sp2}—H = 0.95 Å except, H-atoms attached to O-atoms. Use of riding model for H6 gave a slightly distorted geometry of this H atom. It was thus treated as 'mixed'. At the end of the IAM refinement the R factor was 0.033287, a weighted R factor was 0.100550 and the goodness of fit was 1.07374. Highest difference peak and deepest hole were 0.6 and 0.4e/Å^3 respectively.

2.3. IAM MoPro refinement

The refined model from the previous Olex2 refinement was imported to MoPro (MoPro_1805_win) software package [34]. An Independent Atom Model (IAM) refinement was carried out using a full-matrix least-squares refinement using intensity data up to $Sin\theta/\lambda_{max}$ of 1.125 (Å^{-1}). The data quality was sufficiently good, even for high angles, which allowed us to use all the intensities up to d = 0.45 Å ($\sin\theta/\lambda$ = 1.125 Å^{-1}) resolution (no I/σ cutoff was applied) for the IAM and the subsequent multipolar atom model refinements. The same weighting scheme as used in the previous Olex2 refinement was adopted {$w = 1/[\delta^2(Fo^2) + (aP)^2 + bP]$, where $P = (Fo^2 + 2Fc^2)/3$, with a = 0.0476 and b = 0.0804}. Initially the scale factor was refined followed by the refinement of the position (*x,y,z*) of all atoms and thermal parameters (*Uij*). The bond distances for C—H atoms were constrained to standard values of neutron distances [31]. However, the hydrogen distances obtained from the DFT optimized geometry (Table S3), the details of the optimization procedure are given in the following sections, were found to give a slightly better R factor were used for further MoPro refinements. The anisotropic displacement parameters for H atoms were constrained to calculated values from the SHADE server [35]. The scattering factors for C, H and O are taken from the Atomic Data & Nuclear Data Tables [36] and the refinement was continued till convergence. The residual electron density maps after the IAM refinement was shown in Fig. 2. After IAM refinement with MoPro, the R factor was 0.0481, a weighted R factor was 0.110 and the goodness of fit was 1.421. The minimum, maximum electron-density peaks and rms values were 0.69 and −0.53 and 0.09 eÅ^{-3} respectively.

2.4. Multipolar refinement

The final model from the previous IAM refinement was used for multipolar refinement using MoPro [34] on the basis of the Hansen—Coppens [37] multipolar atom model. According to this

Table 1
Crystallographic and refinement statistics.

Crystal data			
Chemical formula	$C_6H_6O_4$		
M_r	142.10		
Crystal system, space group	Monoclinic, $P2_1/n$		
Temperature (K)	100(1)		
a, *b*, *c* (Å)	3.7649 (1), 18.3527 (4), 8.4839 (2)		
β (°)	96.8300		
V (Å^3)	582.04 (2)		
Z	4		
Radiation type	Mo *Kα*		
μ (mm^{-1})	0.14		
Crystal size (mm)	0.44 × 0.29 × 0.23		
Data collection			
Diffractometer	Bruker D8 Venture, (Bruker 2016)		
Absorption correction	Numerical *SADABS2016*/2 (Bruker,2016/2) was used for absorption correction. w*R2*(int) was 0.1021 before and 0.0507 after correction. The Ratio of minimum to maximum transmission is 0.9304. The λ/2 correction factor is Not present.		
T_{min}, T_{max}	0.698, 0.750		
No. of measured, independent and observed reflections	54,643, 6796, 6085 [> 2.0σ(*I*)]		
R_{int}	0.035		
(sin θ/λ)$_{max}$ (Å^{-1})	1.112		
Refinement			
	(IAM_MoPro)	**(Multipolar_MoPro)**	**(IAM_Olex2)**
$R[F^2 > 2\sigma(F^2)]$, w$R(F^2)$, *S*	0.038, 0.110, 1.14	0.023, 0.040, 1.03	0.033, 0.101, 1.07
No. of reflections	6796	6659	6670
No. of parameters	91	91	97
H-atom treatment	H-atom parameters constrained	H-atom parameters constrained	H atoms treated by a mixture of independent and constrained refinement
Δ⟩$_{max}$, Δ⟩$_{min}$ (e Å^{-3})	0.70, −0.53	0.27, −0.28	0.63, −0.39

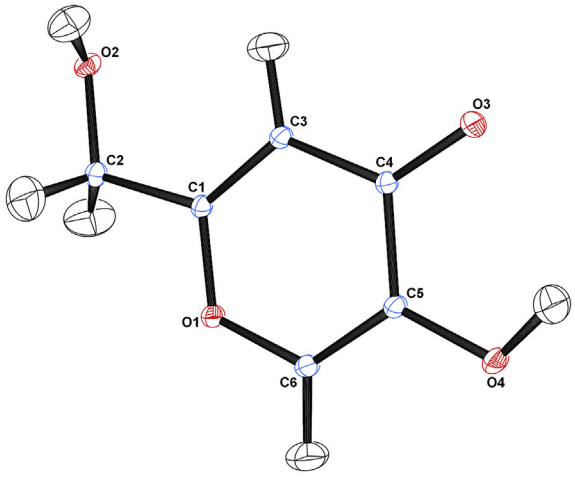

Fig. 1. A thermal ellipsoid diagram of the molecule drawn at 50% probability showing the atom numbering scheme for non-H atoms. The figure is made with ORTEP3 [33].

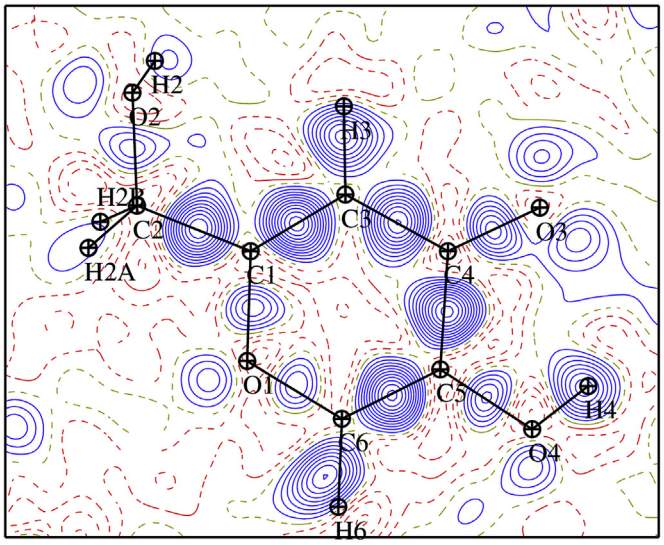

Fig. 2. Residual deformation electron density maps after IAM refinement. Sinθ/λ = 0.7 Å^{-1}..

model, the electron density of pseudo-atoms of molecule are represented by the core electron density (ρ_{core}), valence electron density ($\rho_{valence}$) and the aspherical part of atomic electron density with spherical atom expansion and contraction coefficient κ in the valence shell. The valence electron density is given in term of spherical harmonics, and radial expansion and contraction parameter (κ and κ′) of the valence shell are given in the following equation as Equation (1):

$$\rho(\vec{r}) = \rho_{core}(r) + P_{val}\,\kappa^3\rho_{val}(\kappa r) + \sum_{l=0}^{lmax} \kappa'^3 R_{n_l}(\kappa' r) \sum_{m=0}^{l} P_{lm}\, y_{lm\pm}(\theta,\varphi) \quad (1)$$

Coordinates and thermal displacement parameters of all non-hydrogen atoms were refined using all diffraction data. The same weighting scheme as used in previous sections was used. Resolution dependence of data and model quality was monitored by DRK-plots [38] (Fig. S2). H atoms were treated as in the previous section. Subsequently, the valence population P_{val} parameter and multipole population parameter P_{lm} were refined successively. All the H atoms could be clearly located in the difference Fourier maps. The hydrogen atoms were refined to dipolar level whereas all the other atoms were refined to octopolar level. In the last cycles of the refinement all parameters were simultaneously refined together

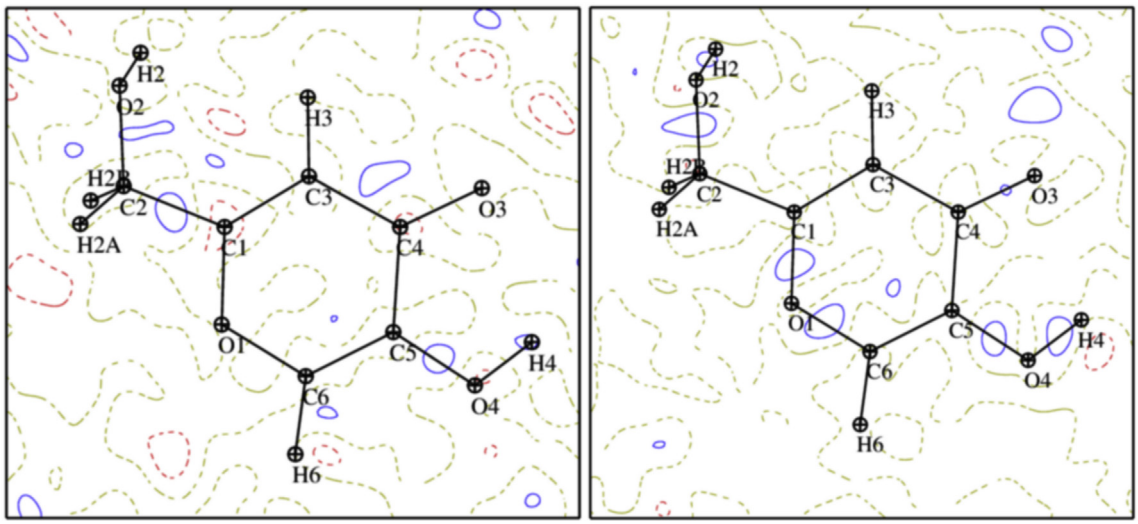

Fig. 3. Residual electron density maps (*a*) Experimental (*b*) Theoretical, after multipolar refinement. Contour level 0.05 e/Å^3. Sinθ/λ = 0.7 Å^{-1}..

until convergence.

As a result of MAM refinement, the R factor was 0.032, a weighted R factor was 0.0398 and the goodness of fit was 0.965. The minimum, maximum electron density peaks and rms values were 0.27 and 0.28 and 0.055eÅ^{-3} respectively. The residual electron density maps are the unique signature to reveal the quality of the refined model. Fig. 3 shows that there is a good agreement between the observed and calculated electron densities of KA molecule.

2.5. Theoretical calculations

A preliminary periodic DFT partial geometry optimization was performed starting with the unit cell and atomic positions obtained from the Mopro IAM refinement. All non-hydrogen atoms in the unit cell were fixed and only hydrogen atoms were allowed to relax during the optimization using the Quantum-Espresso [39] (QE) package. Ultrasoft pseudopotentials were invoked for all atoms using the Perde–Burke–Ernzerh (PBE) [40] exchange–correlation approximation in combination with Grimme's D3 correction for dispersion interactions [41]. The atomic coordinates of hydrogen atoms with fixed lattice constants were relaxed until the forces exerted on the atoms were less than 10^{-4}(a.u) with 10^{-7} (a.u) convergence threshold on total energy. The cutoff energy and electronic density of plane-waves was set to be 60 Ry and 720 Ry respectively. The mesh of the unit cell for k-point sampling was 8 × 2 × 4 which corresponds to ~0.2/Å of k-space resolution. The obtained hydrogen distances were used for further Mopro IAM and MM refinements.

Following multipolar refinement of the experimental model described above using the optimized hydrogen distances, another periodic DFT-D3 single point energy calculation was performed using the all-electron frozen-core PAW [42] approach instead of pseudopotentials. Experimental lattice parameters and atomic coordinates obtained from the multipolar refinements were used as input for QE calculation and were not refined further. The standard PBE PAW atomic data sets were used to describe the wave function and the density in the augmentation spheres. Partial occupancies were calculated using Fermi-Dirac smearing. The electron density was represented on a dense real-space grid comprising of 180 × 432 × 360 points along the crystallographic axes. The mesh of the unit cell for k-point sampling was enhanced to 17 × 3 × 7 which corresponds to the resolution of ~0.1/Å. The cutoff energy and electronic density of plane-waves was set to high to be 70 Ry and 840 Ry respectively to ensure the convergence and accuracy. The all-electron charge density (valence and core) was obtained in cube file format using *pp.x* package of QE. The Fourier transform of electron density was performed to obtain the static theoretical structure factors up to the experimental sin θ/λ limits using a python script developed by one of us (AM) and is available via email. The multipole refinement was performed using Mopro on the charge density reconstructed from these theoretical structure factors and results are represented here as "Theoretical". During the MM refinement using theoretical structure factors, the thermal parameters of atoms were set to zero and only scale factor and charge density parameters were refined.

3. Results and discussion

3.1. Static electron density and crystal packing

Fig. 4(a and b) shows the static electron density maps for the experimental and theoretical. It can be noticed that the lone pairs on O1, O2 and O4 atoms have been concentrated as a single lobe while the lone pairs on O3 atom have bi-lobed structure as viewed along the plane of the aromatic ring. Infact the lone pairs of all the oxygen atoms are coplanar with the plane of the aromatic ring. These findings are consistent with the literature [43].

KA (5-hydroxy-2-(hydroxymethy1)- γ-pyrone) is a polyfunctional heterocyclic molecule consisting of -CH2OH, a keto group and a hydroxyl substituent attached to the heterocyclic ring. This oxygen carrying skeleton acts as an important reaction centre that enables to proceed several types of reactions like oxidation, reduction, alkylation, acylation, nucleophilic/electrophilic substitution reactions and ring opening of the molecule [44]. Beside these, the two ring hydrogen atoms are also present which lead to a large number of possible tautomers. (Fig. 1). The O3 of carbonyl oxygen or Oxo-group in the heterocyclic planar pyran ring of the KA molecule is tilted towards 5-hydroxy as the angle O3C4C5 is 119°(1) significantly smaller than O3C4C3 which is 125°(1).This could be due to presence of a weak intra-molecular hydrogen bond between O4–H4···O3 at a distance of 2.239 Å. Among the two hydroxy groups of the KA, the 5-hydroxy O4–H4 attached with pyrone ring is planar whereas the methyl hydroxy O4–H4 is 106.26°out of the plane. This hydroxyethyl (-CH2OH) moiety has been found

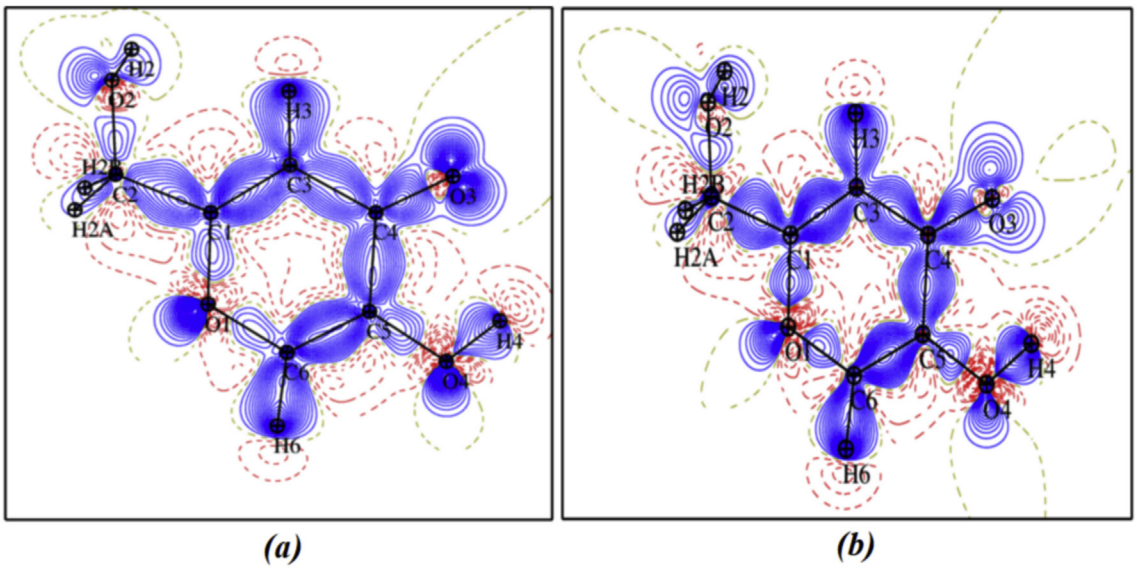

Fig. 4. Static deformation density maps after multipolar refinement (***a***) Experimental (***b***) Theoretical using all data: contour 0.05 e/Å^3. The O2 atom is slightly out of the plane, hence density seems diminished.

important in determining the conformational transformations of the two conformers of KA differ from each other by 120° rotation [45]. Thus, the flexible structure of KA is important to determine the possible tautomer as well as their corresponding rotamers. However, the present molecular structure of KA is the tautomeric form I. The unit cell packing along *c*-axis is shown in Fig. 5.

3.2. Hirshfeld surface and fingerprint analysis

The ability to bindthe enzyme-substrate complexe is primarily because of the intermolecular interactions participating in. So, it is important to have the knowledge of interacting surface of the substrate/drug molecule facilitating this binding in the respective biological environment. Here, in the present study to understand the anti-Tyrosinase ability of KA the Hirshfeld surface is instrumental to visualize the intermolecular interactions of the molecule in its crystalline phase. Fig. 6 shows the Hirshfeld surface view of

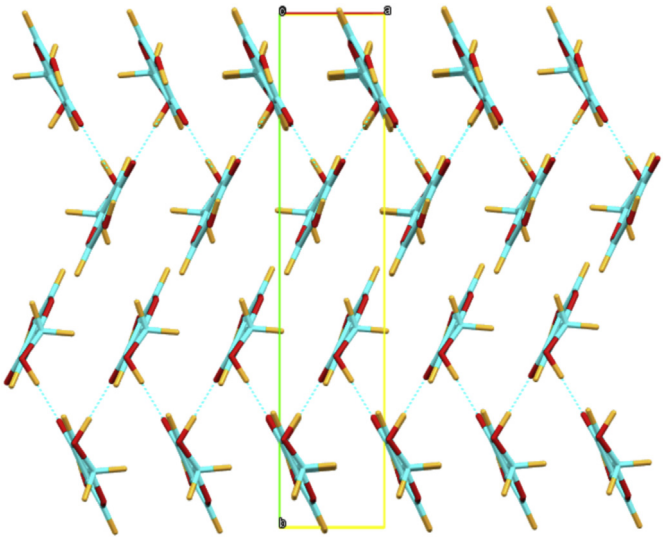

Fig. 5. A herringbone molecular arrangement with packing along *c*-axis.

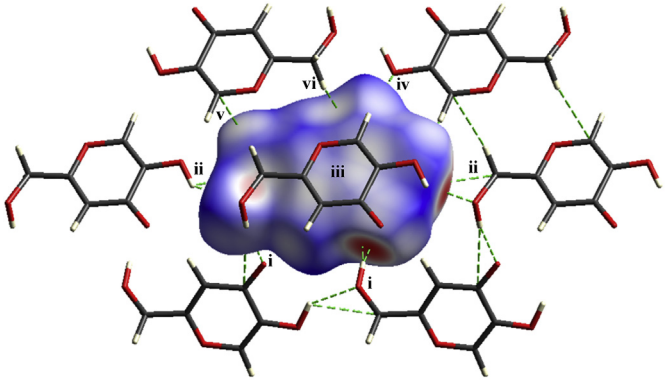

Fig. 6. A Hirshfeld surface of the parent molecule, showing the interacting molecules. The symmetry codes are same as in Table 2.

the intermolecular interactions formed in the KA molecule used to bind with its biological environment. *Crystal Explorer* [46] was used to map the Hirshfeld surface of KA molecule. The indications of colours in the molecular environment of the crystal space are useful to identify the possible intermolecular interactions formed by the KA molecule with the active site of Tyrosinase enzyme. The contacts shorter than the sum of the van der Waals radii are coloured deep red on the surface. The white coloured contacts are close to the length of the van der Waals radii limit while the longer contacts are represented by the blue color [47]. The surface map shows the dark red region at the vicinity of O3, O4 and O2 depicting the presence of strong O2–H2···O3^{i}, O4–H4···O2^{ii}, C2–H2B···O2^{iii}, C6–H6···O4^{iv} intermolecular interactions (Symmetry codes are same as in Table 2).

The fingerprint plots illustrate the highest proportion of O···H interactions for all the structure of KA studied making up the majority of the surface by contributing 52.1%. The combined reciprocal O···H interactions are represented as spikes in Fig. 7. The H···H interactions make up the 24.5% of the total surface While the C···H and O···C interactions make up 9.4% and 7.1% respectively from all the surface. The C···C interactions contribute 4.9% and O···O interactions make up 2% of the total surface in the KA molecule. So,

Table 2
Hydrogen-bond geometry (Å, °) for (Multipolar_MoPro).

D—H···*A*	*D*—H	H···*A*	*D*···*A*	*D*—H···*A*
C2—H2*B*···O2^{i}	1.10	2.33 (1)	3.3818 (3)	159 (1)
O4—H4···O2^{ii}	1.00	1.91 (1)	2.7203 (2)	136 (1)
O4—H4···C2^{ii}	1.00	2.57 (1)	2.9774 (2)	105 (1)
O4—H4···O3	1.00	2.24 (1)	2.7219 (2)	108 (1)
C6—H6···O4^{iii}	1.09	2.29 (1)	3.3358 (3)	161 (1)
O2—H2···O3^{iv}	1.01	1.68 (1)	2.6726 (2)	168 (1)
O2—H2···C4^{iv}	1.01	2.59 (1)	3.5782 (2)	168 (1)

Symmetry codes: (i) *x*-1, *y*, *z*; (ii) *x*, *y*, *z*-1; (iii) -*x*, -*y*+1, -*z*; (iv) *x*-1/2, -*y*+1/2, *z*+1/2.

the Hirshfeld surface map and the individual contributing interaction from the total percentile demonstrates the characteristic intermolecular interactions as well as their strength in the KA molecule.

3.3. Topological analysis of electron density

The study of topological features of a molecule enables to understand the details about the strength of intermolecular interactions rather than depending merely on the geometry of the molecule. A bond critical point (BCP) search was carried out to analyse quantitatively the electronic structure of KA molecule [48]. The BCPs search for all the bond of KA molecule invariably found (3, −1) BCPs, confirming the presence of covalent interactions. The electron density as well as the Laplacian of electron density at all the BCPs were calculated and compared with the corresponding Theoretical values of all the bonds in the KA molecule (Table S1). The molecular graph in Fig. S3 locate the covalent BCPs in the bonds of KA molecule.

3.4. Electron density

The electron density ρ (bcp) is the physically observable quantity which is found to be maximum near the nucleus and minimum elsewhere [49] and is used to determine the bonding situation as well as the chemical reactivity of the molecules [50]. The position of BCPs in the KA molecule give the idea of the polarity of the bonds in the molecule. Therefore, the position of BCPs of homonuclear C—C bonds are at the middle of the bonds while the position of BCPs of heteronuclear bonds (C—H, C—O, O—H) are staying away from the middle and are close to the either electropositive atom from all the BCPs of KA molecule (Fig. S3).

From all the homonuclear C—C bonds of KA molecule the $\rho_{BCP}(\mathbf{r})$ of C5—C6 (2.353/2.287 e/Å^{-3}) and C1—C3 (2.285/2.215 e/Å^{-3}) have the highest values of electron density at their BCPs. This higher concentration of electron density shows that the charge density has been shifted towards the BCPs of C5—C6 and C1—C3 from the neighboring bonds of the pyrone ring. The position of conjugated double bonds at these BCPs also confirm that the parent KA molecule possesses the tautomeric form I [51] from all the possible VIII tautomeric forms of KA molecule. While the electron density $\rho_{BCP}(\mathbf{r})$ of the adjacent bonds in the pyrone ring C5—C4 and C3—C4 is

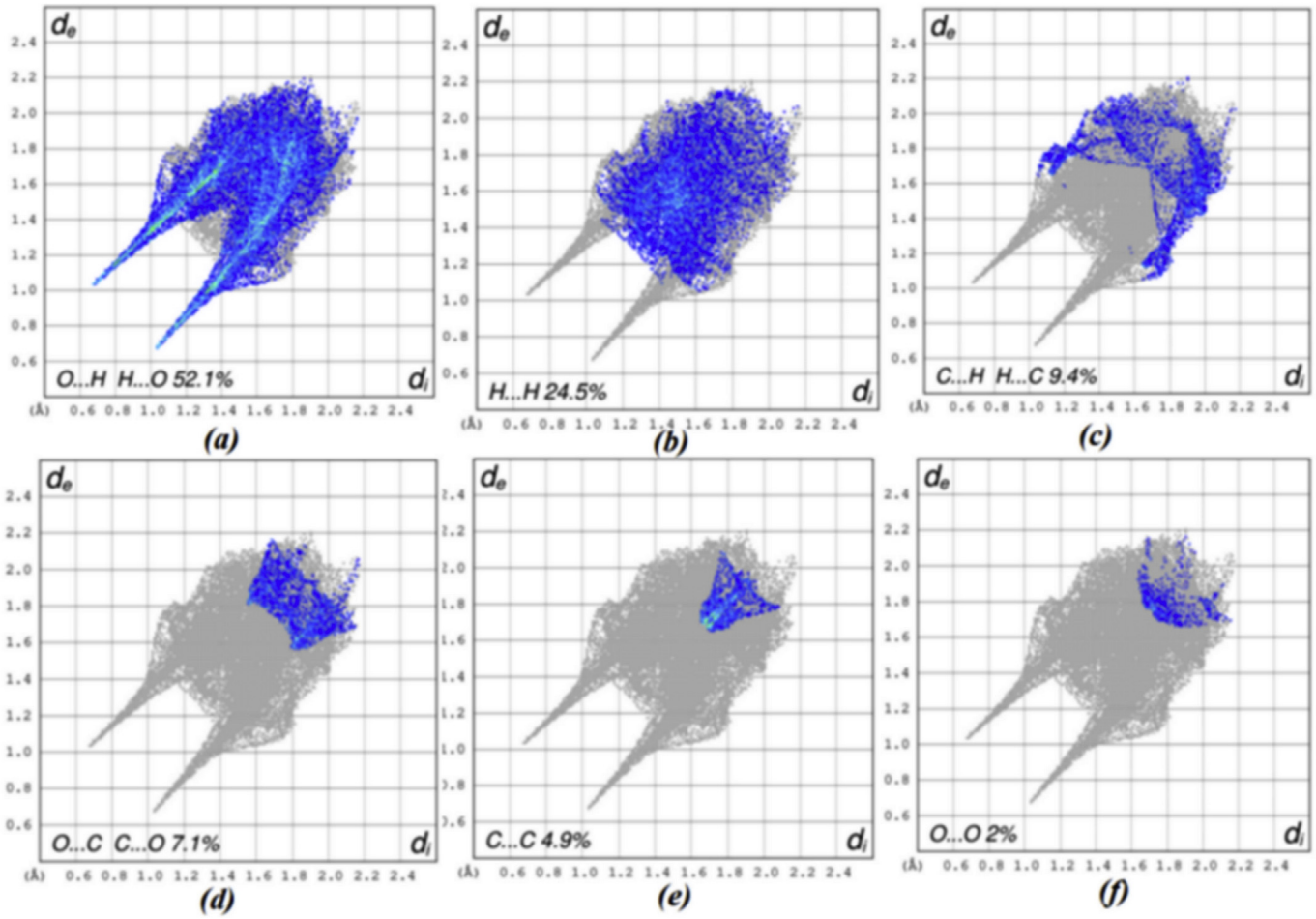

Fig. 7. Fingerprint plots showing the percentages of interactions present in the molecule.

found to be (1.976/1.887 e/Å^{-3}) and (1.947/1.875 e/Å^{-3}) respectively. While the electron density $\rho_{BCP}(\mathbf{r})$ of C1—C2 is found to be smaller (1.747/1.696 e/Å^{-3}) from all the C—C bonds of KA molecule. This smaller values of electron density at their BCPs may be due to the adjacent methoxy (-CH2OH) group in the KA crystal.

From the heteronuclear C—O bonds, the carbonyl C4═O3 have the highest values of electron density $\rho_{BCP}(\mathbf{r})$ (2.647/2.647 e/Å^{-3}) at their BCPs with the smallest values of bond length (1.250/1.250 Å) in the pyrone ring. Apart from this, the $\rho_{BCP}(\mathbf{r})$ of the adjacent C1—O1have higher values of $\rho_{BCP}(\mathbf{r})$ (2.045/2.005 e/Å^{-3}) than C6— O1 (1.942/1.924 e/Å^{-3}). This higher electron density value can be illustrated because of the neighboring methoxy group in the KA molecule. The C5—O4 have higher values of electron density (2.093/2.065 e/Å^{-3}) because of the neighboring 5-hydroxy at the pyrone ring. The smaller electron density values (1.801/1.777 e/Å^{-3}) of C2—O2of the methyl hydroxy suggests the nucleophilic substitution of a variety of anions like by replacing the hydroxyl group.

Among the hydroxyl groups O—H, 5-hydroxy O4—H4 have higher values of electron density $\rho_{BCP}(\mathbf{r})$ (2.353/2.169 e/Å^{-3}) at their BCPs than that of the electron density of methyl hydroxy O2—H2 (2.294/2.138 e/Å^{-3}) of the pyrone ring in the KA molecule. It is worth mentioning that The out of plane hydrogen H2 is responsible for producing a huge diversity of KA derivatives by favoring removal of hydroxyl group resulting the nucleophilic substitution of huge variety of anions giving iodokojic acid, azidokojic acid, thiocyanato and isothiocyanato Kojic acid and Chlorokojic acid [52—54]. From the derivatives of Kojic acid, the charge density of Chlorokojic acid has been studied [53]. The out of plane chlorine of the KA derivative is also because of the out of plane H2 of the Kojic acid. The above facts support a detailed structure analysis of the parent molecule KA.

3.5. Laplacian of electron density $\nabla^2\rho_{cp}(r)$

The Laplacian, which is the sum of the second derivatives of electron density $\nabla^2\rho_{cp}(\mathbf{r})$ provides ample information to understand the chemical nature of a molecule. The experimental Laplacian $\nabla^2\rho_{cp}$ of electron density of KA molecule was calculated and compared with the corresponding theoretical values (Table S1). All the atoms of the chemical bonds of KA molecule have the closed shell interactions as the Laplacian values have been found to have $\nabla^2\rho_{cp}(\mathbf{r}) < 0$. Fig. 8 shows the Laplacian map of the KA molecule.

In the present study, the C5—C6 and C1—C3 chemical bond in the pyrone ring have the higher concentration of the Laplacian of electron density $\nabla^2\rho_{cp}(\mathbf{r})$ −25.330/-21.230 eÅ^{-5} and -23.910/-19.400 eÅ^{-5} from all the C—C bonds in the KA molecule. From the adjacent C3—C4 and C4—C5 bonds, the Laplacian of electron density $\nabla^2\rho_{cp}(\mathbf{r})$ of C4—C5 is −17.860/-14.200 eÅ^{-5} higher than C4—C5 -17.860/-14.200 eÅ^{-5} this might be due to the ketonic carbonyl at C4 and the hydroxyl group attached with the C5 of the pyrone ring. The C1—C2 have the smallest values −13.720/-10.670 eÅ^{-5} of their Laplacian of electron density $\nabla^2\rho_{cp}(\mathbf{r})$ as the electron density has been shifted to the adjacent methyl hydroxy group.

From the C—O bonds in the pyrone ring of the KA molecule, the C1—O1 have higher values −20.340/-14.160 eÅ^{-5} of the Laplacian electron density $\nabla^2\rho_{cp}(\mathbf{r})$ than C6—O1 -18.500/-11.390 eÅ^{-5} (Fig. 9). Whereas the $\nabla^2\rho_{cp}(\mathbf{r})$ at the *bcps* of C5—O4 is −21.050/-14.100 eÅ^{-5}. The concentration of electron density is because of the neighboring hydroxyl group. The C2—O2 bond have the smallest $\nabla^2\rho_{cp}(\mathbf{r})$ value −12.620/-6.500 eÅ^{-5} because of the *trans*-hydroxy methyl group. From the above all, the only O3C4═O3 *keto* group have the highest value −29.270/-29.530 eÅ^{-5} of Laplacian of electron density at the *bcp* in the KA molecule.

There are two hydroxyl groups that are responsible for determining the conformations in the KA molecule. The 5-hydroxy O4—H4 has a slightly higher concentration of the electron density with the Laplacian $\nabla^2\rho_{cp}(\mathbf{r})$ −24.680/-24.810 eÅ^{-5} while the Laplacian of electron density of methyl hydroxy O2—H2 is −22.400/-22.630 eÅ^{-5}. The O4 and H4 atoms have also got slightly more negative atomic charges than the O2 and H2 atoms. The slightly higher concentration of negative charge on C5-hydroxy group can be because of its vicinity to the electron rich aromatic ring. However, the Laplacian profiles of both models exhibit equal charge separations and identify same type of interactions. The Laplacian profiles also show that in case of C4—O3 bond, the bond critical points is more towards the carbon atom as compared other hydroxy C—O bonds which suggests that in case of hydroxyl, the oxygen atom is deficient in electrons and attracts the shared electron more towards itself. The positions of the *bcp* for C—O and O—H bonding interactions almost is in agreement between experiment and theory as can be seen in Fig. 9.

From the C—H bonds of the KA molecule, the C6—H6 and C3—H3 are attached to the pyrone ring with the Laplacian of electron density $\nabla^2\rho_{cp}(\mathbf{r})$ at their bcps −18.620/-17.420 eÅ^{-5} and -15.830/-

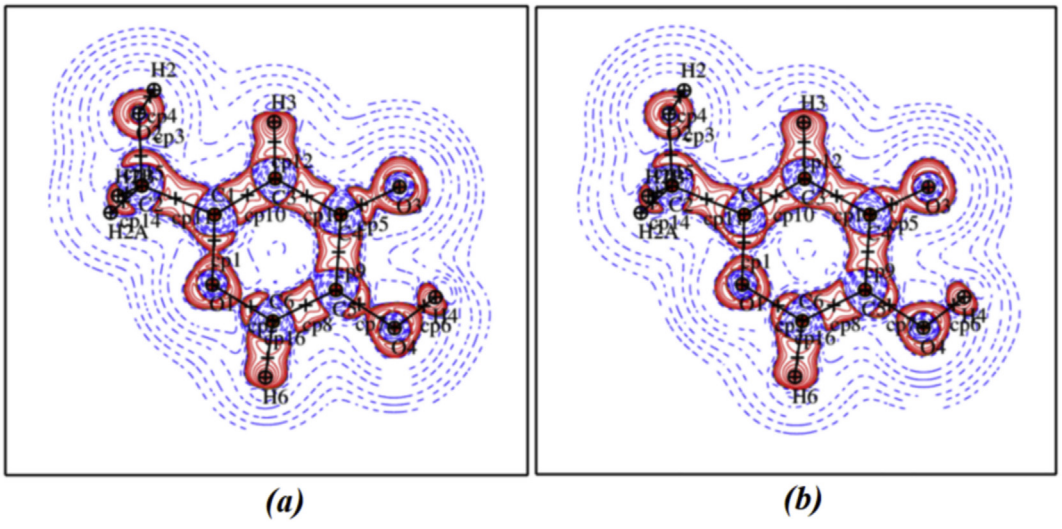

Fig. 8. Laplacian of electron density maps for the (a) experimental (b) Theoretical model showing the covalent bond critical points.

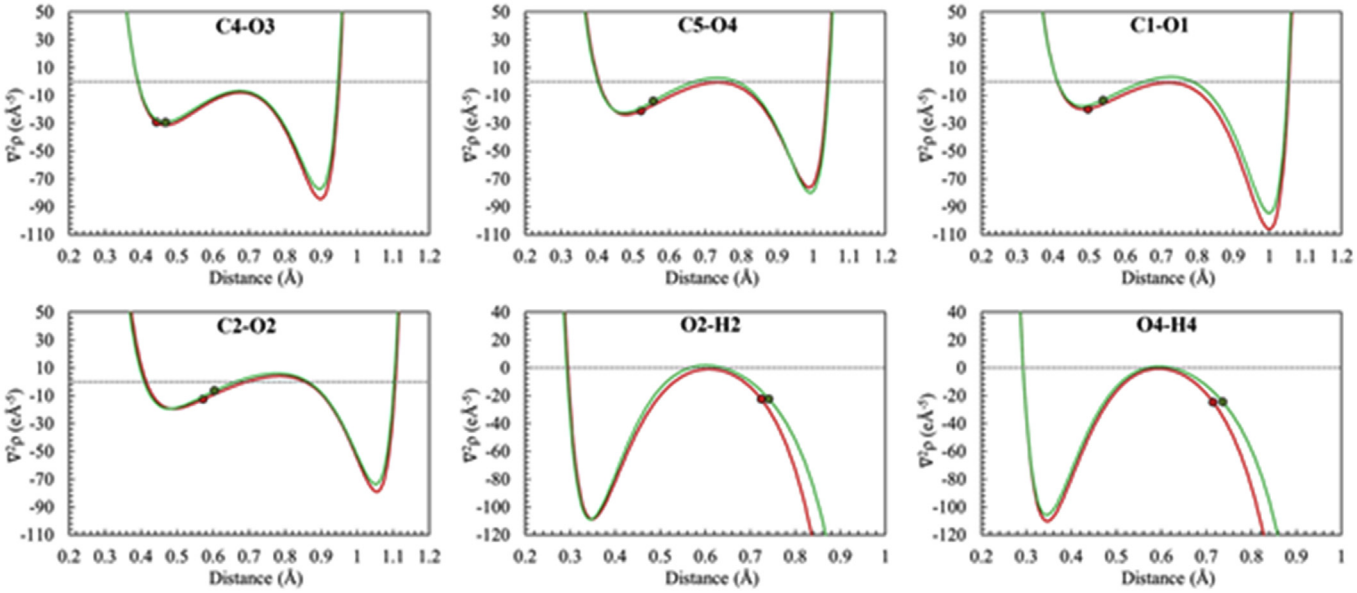

Fig. 9. The Laplacian profiles of oxygen related covalent bonds from theory and experiment.

15.240 eÅ^{-5} respectively. The higher electron density of C6—H6 is because of the locally presence of oxygen of pyrone ring while the relatively smaller Laplacian values at the bcps of C3—H3 may be because of the electron withdrawing carbonyl of the keto group in the KA molecule. While the methyl hydrogens C2—H2A and C2—H2B have the Laplacian of electron densities −13.670/-14.960 eÅ^{-5} and -14.870/-14.640 eÅ^{-5} respectively at their *bcps*.

3.6. Topological characterization of intermolecular interactions

The oxygen containing polyfunctional skeleton of KA molecule has the ability to form intermolecular interactions with the neighboring symmetry mates in the crystal. The critical point search for the closed shell intermolecular interactions are listed in Table S2. The bonding nature for each of these interactions is verified both by the bond of each atom and their virial paths [55,56] (Bader 1990, 1998). The topological analysis of these interactions shows that they have positive values of Laplacian at their bcps $\nabla^2\rho_{cp}(\mathbf{r}) > 0$ [57,58] confirming the presence of closed shell interactions. The classical O—H···O hydrogen bonding interactions join the four symmetrically sitting molecules in the asymmetric unit of KA crystal in which each of the two molecules are joined via O2—H2•••O3^{i} and O4—H4•••O2^{ii} type of intermolecular interactions. The O2—H2•••O3^{i} hydrogen bonding interaction (1.679 Å) joins with the electron density $\rho_{bcp}(\mathbf{r})$ 0.274/0.286 eÅ^{-3} and the corresponding Laplacian of electron density $\nabla^2\rho_{cp}$ is 2.749/3.624 eÅ^{-5} whereas the bond kinetic and potential energy density values are 86.040/104.670 and −97.190/-110.630 KJ/mol/Bohr^3 respectively [i = *x*-1/2, -*y*+1/2, *z*+1/2]. Whereas the O4—H4•••O2^{ii} (1.909 Å) has the electron density value 0.180/0.178 eÅ^{-3} with the Laplacian of electron density $\nabla^2\rho_{cp}$ 2.188/2.432 eÅ^{-5} while the kinetic and potential energy density values are found to be 57.680/61.700 and −55.770/-57.150 KJ/mol/Bohr^3 respectively [ii = *x*, *y*, *z*-1]. The electron density and Laplacian of electron density values suggest incipient or partial covalent bonding character of these two hydrogen bonds [59—61] in the KA molecule. The O—H···O interactions have almost equal values of $\boldsymbol{\lambda_1}$ and $\boldsymbol{\lambda_2}$ eigenvalues whereas the parallel curvature $\boldsymbol{\lambda_3}$ is 4 order of magnitude greater than the two. Similarly the ellipcity (ε) values are also greater than zero as expected of a polar bond.

All the C—H•••O interactions have a lower electron density at their BCPs than the above mentioned O—H•••O but have a positive Laplacian. The $\rho_{bcp(r)}$ values range from 0.077 e Å^{-3} to 0.027 e Å^{-3} which are well within the interval as described by Koch and Popelier [73] for CH•••O type hydrogen bonds. Among all the C—H•••O interactions in the KA molecule, the C2—H2B•••O2^{iii} (2.330 Å) is found to have the highest values of electron density 0.077/0.077 eÅ^{-3} and Laplacian of electron density1.044/1.061 eÅ^{-5} whereas the corresponding kinetic and potential energy values are 23.370/23.590 and −18.290/-18.280 KJ/mol/Bohr^3 respectively. The C—H···O interactions have almost equal values of $\boldsymbol{\lambda_1}$ and $\boldsymbol{\lambda_2}$ eigenvectors however the parallel curvature $\boldsymbol{\lambda_3}$ is almost 1 order of magnitude greater than the two. Similarly the ellipcity (ε) values are also greater than zero but not as high as for O—H···O interactions showing that the bonds are less polar. All other hydrogen bonds listed in Table S2 are weaker and belong to the closed-shell interaction type. A cluster of the interacting molecules with the parent molecule showing the bond paths and intermolecular critical points is shown in Fig. 10.

3.7. The homonuclear weak intermolecular interactions

The weak interactions play significant role in the biological system. In the present study, weak homonuclear interactions particularly C(π)•••C(π), H•••H and O•••O type have been observed. It is to be noted that these kind of interactions are not observed in the charge density study of Chloro Kojic acid [53]. The π-cloud of carbon atoms *p*-orbitals in the heterocyclic aromatic ring are involved in the C5•••C6^{iii} and C3•••C1^{v} intermolecular interactions with it symmetrically sitting neighboring molecule. The bond path of C5•••C6 is comparatively longer (3.369 Å) than C3•••C1(3.363 Å), having smaller electron density of 0.044/0.037 e/Å^{-3}. These π•••π interactions significantly contribute in the molecular packing of KA.

The H•••H interactions have solicited significant interest over the last several years [62]. These special types of dihydrogen bonding interactions favor the local stabilization of the molecule in the crystal environment and occurs between those hydrogen atoms

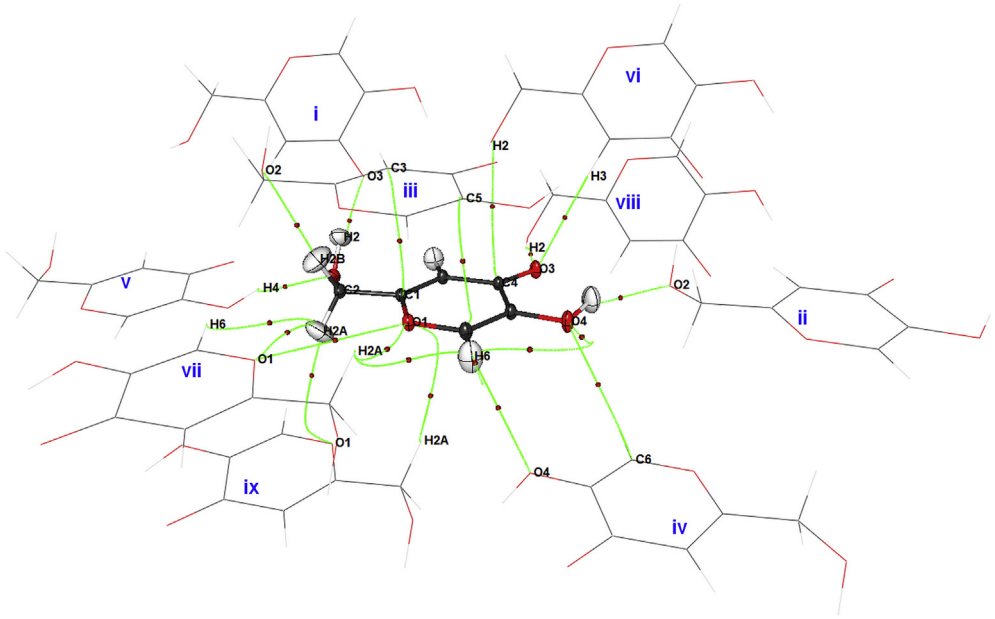

Fig. 10. A molecular cluster showing the bond paths (green) and intermolecular critical points (crimson). Symmetry codes: (i). x-1/2; -y+1/2; z+1/2; (ii). x, y, z-1; (iii). x-1; y; z; (iv) -x; -y+1; -z; (v). x; y; z+1; (vi). $x+1/2$; $-y+1/2$; $z+1/2$ (vii) -x; -y+1; -z+1; (viii). x-1/2; -y+1/2; z+1/2; (ix) $x+1/2$; $-y+1/2$; $z+1/2$.

having similar charges and electronic environment [63]. We have identified the H2A···H6^{ix} and H6···H6^{iv} short contacts in the KA molecule with an average distance of 2.6 Å and exhibit the characteristic of closed-shell interactions with small electron density values of 0.027/0.030 and 0.025/0.029 e/Å^{-3} with the corresponding small positive Laplacian values of 0.358/0.384 and 0.336/0.366 e/Å^{-5} respectively. The O1···O1^{ix} weak interactions are also found to be present in the KA molecule having bond length of 3.485 Å with a smaller positive Laplacian of 0.233/0.244 e/Å^{-3}. These homonuclear intermolecular interactions contribute in the molecular packing of the KA molecule. These types of interactions reveal the tendency of forming interaction with the polar residues/moieties of Tyrosinase enzyme resulting in inhibition of Melanogenesis which has been confirmed in Fig. S 4 and S5 [PDB code: 3NQ1] [64].

3.8. Gradient vector field and atomic charges

The electron density of a molecule is a scalar quantity and can be expressed as the gradient vector field too. The gradient vector field $\nabla\rho(r)$ of KA was plotted using VMoPro program as shown in Fig. 11 The *basin* [65] is the boundary of each atom participating in the whole molecule of the crystal surrounded by zero flux surface where the gradient trajectory terminates stemming from the saddle point. The Bader's AIM atomic charges of atoms in the KA were experimentally and theoretically calculated using WinXPRO v.3x [66]. The values are in good agreement in determining the chemical nature as well as the bonding environment of the molecule (Table 3). The electropositive carbon atoms have small volume and resemble the prismatic form while the highly electronegative oxygen atoms occupy large volume and resemble like a drop except the oxygen of pyrone ring. In the pyrone ring of the KA molecule, the O3 of the *Oxo*-group is found to have highest values of the polarity of negative charges [-1.013/-0.868e] with the expected larger volume of [16.69/16.06 Å^3]. This high negative charge tends to have high positive charge [0.799/0.773e] in its attached C4 atom with the atomic volume [7.233/7.170 Å^3] making the bond O3═C4 more polar. This high polarity of charge is responsible for establishing the classical strong hydrogen bonding interactions in the KA molecule that might be instrumental in its binding with the active site of Tyrosinase enzyme resulted in the inhibition of melanin. In the case of O1 of the pyrone ring, the situation is quite different. The O1 carries the higher concentration of negative charge [-1.049/-0.808e] with a smaller volume [14.450/13.830 Å^3]. While the adjacent C1 and C6 of the pyrone ring carries atomic volumes [8.444/8.139 Å^3] and [10.120/9.824 Å^3] with the corresponding polarity of charge [0.322/0.389e] and [0.354/0.335e] respectively. There is an unequal distribution of charges between the C1 and C6 attached with O1 of the pyrone ring. The O1—C1 bond is comparatively more polar as the charges are more concentrated towards C1 than that of C6. Among the two hydroxyl groups, the O4 carries higher values of charges [-0.904/-0.809e] with the expected higher volume of [16.160/15.710 Å^3] than that of O2 having the charge [-0.881/-0.837e] with corresponding atomic basin of [15.46/15.09 Å^3]. The charge of hydrogen atom H4 is more positive [0.502/0.480e] having smaller volume [2.863/3.210 Å^3] because it is bound with higher electronegative O4 atom than that of H2 bound with O2. The hydrogen atoms in the KA molecule show a significant difference in their charges as well as corresponding volumes.

This high negative charge of O3 tends to have high positive charge in its attached C4 with the corresponding atomic volume is making the bond O3—C4 more polar. It is to be noted that the concentration of the negative charges on the O1 and O3 oxygens in the pyranone ring is same but the there is a significant difference in their atomic volumes. This difference in the atomic charges with respect to the volume occupied by each of the pyrone oxygen can be explained by the fact of the polarization of atomic charges. Moreover, O1 has a lower atomic volume as it is an endocyclic atom, that is, because it is necessarily more crowded than an exocyclic = O group. As the concertation of the charges are same but the accumulation of the charges per unit area is different in case of O1 results to squeezed compensate its atomic volume only (higher atomic charge does not always suggest larger atomic volumes). Alternatively, among the two hydroxyl groups of KA molecule, O2 and O4 have atomic charges values [-0.881/-0.837e] and [-0.904/-0.809e] while the corresponding values of their atomic charges are [15.46/15.09 Å^3] and [16.16/15.71 Å^3] respectively. Here, it can be

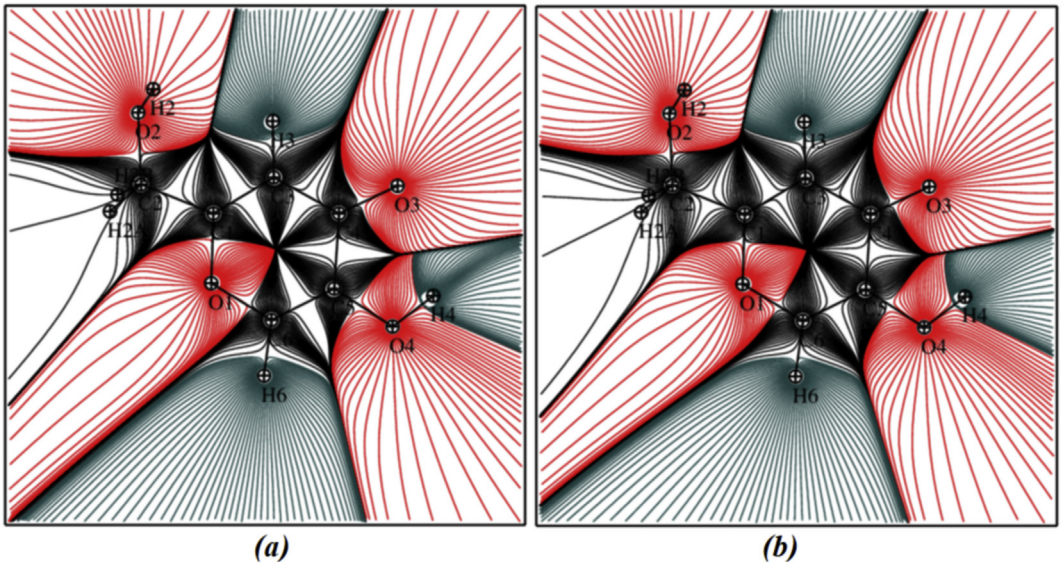

Fig. 11. The gradient vector fields showing the atomic basins of individual atoms for (*a*) experimental and (*b*) Theoretical model.

Table 3
Atomic Charges and atomic volumes.

Atom	Charge (q)		Volume (Å^3)	
	MM_{Exp}	MM_{Theo}	MM_{Exp}	MM_{Theo}
O1	−1.049	−0.808	14.45	13.83
O2	−0.881	−0.837	15.46	15.09
O3	−1.013	−0.868	16.69	16.06
O4	−0.904	−0.809	16.16	15.71
H4	0.502	0.480	2.863	3.210
C5	0.508	0.432	8.017	8.323
C1	0.322	0.389	8.444	8.139
C3	0.049	0.028	11.23	11.08
H3	0.073	0.028	7.168	7.368
C2	0.532	0.386	7.313	7.281
H2A	0.045	−0.007	5.960	6.475
H2B	0.053	−0.002	5.829	6.301
C6	0.354	0.335	10.12	9.824
C4	0.799	0.773	7.233	7.170
H2	0.438	0.418	3.255	3.038
H6	0.136	0.073	5.656	6.202

seen that the 5-hydroxy oxygen has higher values of atomic charge as well as the respective atomic volume than that of the oxygen of methyl hydroxy. The volume of the oxygen atoms are of the order of O3>O4>O2>O1. Among the carbon atoms of the pyrone ring in the KA molecule the C4 carries the most electropositive character with atomic charge [0.799/0.773e] while the atomic volume is [7.233/7.170 Å^3].

3.9. Electrostatic potential and binding affinity

The electrostatic potential (ESP) distributions particularly indicate that how the molecule will approach and consequently bind with the biological receptors or ligands in the active site of enzymes [16–24,67–70] This approach includes the fact that the molecule of the crystal has the ESP complementary to the ESP of the receptor site, sitting in with the help of intermolecular interactions and can be considered to have the similar ESP properties to those of the receptor and is responsible for recognition of molecules in the biological environment [71]. It paves the way to physically observe the nucleophilic and electrophilic centres where the chemical reactions are expected to happen. The Su & Coppens (1992) [72] method was used for the generation of ESP surface map. The isosurface representation of both the experimental and theoretical calculations KA molecule is shown in Fig. 12. Although a theoretical calculation of ESP of KA molecule has previously been reported at gas-phase and aqueous solution [51] but the report was lacking the details at solid-phase. Both the experimental and theoretical ESP maps represent the large negative ESP region in the vicinity of O2, O3, O4 and O1 of the pyrone ring skeleton of KA molecule (see Fig. 13).

Based on the structure of Tyrosinase enzyme deposited in PDB (3nQ1) [64], one of the most important ligand-receptor interactions

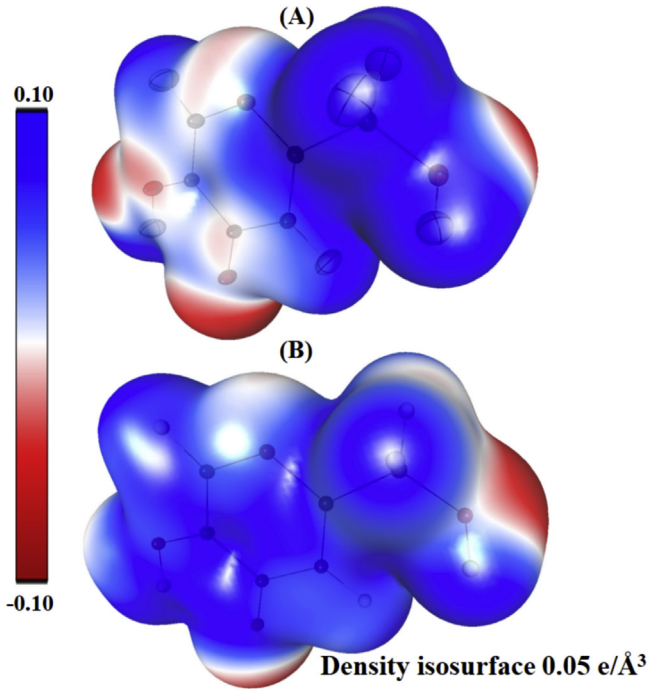

Fig. 12. A three-dimensional electron density surface of the molecule coloured according to the electrostatic potential. (A) Experimental (B) Theoretical: contour level 0.05 e/Å^3.

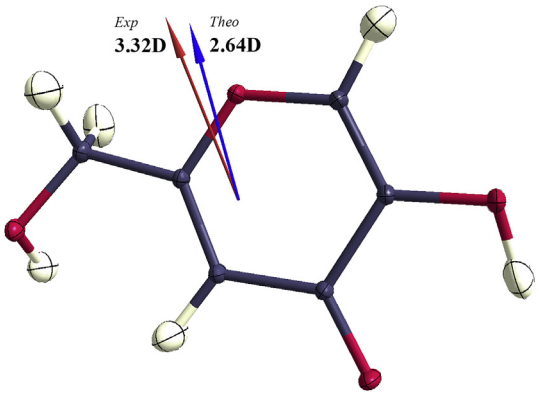

Fig. 13. Total dipole moment for the molecule computed from experimental (red) and theoretical (blue) models.

is the hydrogen bonding of the following types (i) the keto oxygen O3 of γ-pyrone act as donor to asparagine and phenylalanine, and acceptor to glycine (ii) a π•••π cloud of pyrone ring with the asparagine residue with the active site of Tyrosinase enzyme (iii) the oxy-substituents forms interaction with the N of the arginine residue and also with the proline. Because of the low resolution of 2.3 Å of the Tyrosinase enzyme leaves some ambiguity in the other related interactions, hence we may obtain plausible features to measure the strength of likely hydrogen bonds so to understand the KA-Tyrosinase complex. However, it may also be worth to suggest that the KA can form possible eight tautomers and each one can form corresponding rotamers. Because of the *C*—OH bond rotation, the correct rotamer being used to bind would also change the ESP features complementary with it as in the present case tautomeric form I to be considered.

The negative ESP around the γ-pyrone ring is due to the negative charge contribution of oxygen atom of the ring as well as the adjacent keto-oxygen in the KA molecule. This negative ESP region of the γ-pyrone ring facilitates the embedding of KA in the active site of Tyrosinase enzyme. The keto-oxygen O2 has higher ESP values and is responsible for strong hydrogen bonding of KA molecule to bind with the active site of Tyrosinase enzyme thus actively inhibiting its melanin producing activity and preventing the skin from the nuisance of melasma.

The total dipole moment for both the experimental and theoretical models of the KA was calculated as sum of the individual atomic dipole contributions using MoProViewer (Guillot, 2011) The dipole moment values for both the models were 3.32D and 2.64D respectively. The Experimental dipole moment value have been found slightly higher than the theoretical. Due to presence of electronegative oxygen atoms at scattered locations in the molecule, the negative charge is not concentrated at a single region; the polarity of the molecule is not so high.

4. Conclusions

A detailed analysis of the distribution of charge density in tyrosinase inhibitor kojic acid provides insight into its anti-melanogenesis role. Through a complementary analysis of the deposited structures in PDB, it becomes evident that it forms strong hydrogen bonds with those residues of the enzyme which are located at the entrance of active site. It is found that it forms a strong hydrogen bond with one of the water molecules close to the metal atoms. It is assumed that this water molecule might be crucial for melanogenesis which is hampered by hydrogen bonding with Kojic acid. However, since the molecule exists in a number of tautomeric forms, it will be desirable to study the enzyme-inhibitor complex at a crystallographic resolution where the hydrogen atoms can be ascertained experimentally.

Author contribution

Maqsood Ahmed and Sajida Noureen originally devised the project and procured the materials. Asma Hasil prepared the samples and the initial draft. Maqsood Ahmed collected the diffraction, solved and refined the structure. Arshad Mehmood carried out theoretical calculations and wrote down the theoretical section. All the authors reviewed the manuscript.

Declaration of competing interest

The authors declare no competing interests.

Acknowledgement

The authors gratefully acknowledge the Materials Chemistry Laboratory, Department of Chemistry, The Islamia University of Bahawalpur, Pakistan for the provision of research facilities. The Materials Chemistry Laboratory was established with a funding from the Higher Education Commission of Pakistan.

Appendix A. Supplementary data

Supplementary data to this article can be found online at https://doi.org/10.1016/j.molstruc.2020.128295.

References

[1] S.H. Lee, S.Y. Choi, H. Kim, J.S. Hwang, B.G. Lee, J.J. Gao, S.Y. Kim, Mulberroside F isolated from the leaves of Morus alba inhibits melanin biosynthesis, Biol. Pharm. Bull. 25 (8) (2002) 1045–1048.
[2] R.A. Spritz, V.J. Hearing, Genetic disorders of pigmentation, Adv. Hum. Genet., Springer1994, pp. 1-45.
[3] X. Lai, H.J. Wichers, M. Soler-Lopez, B.W. Dijkstra, Structure of human tyrosinase related protein 1 reveals a binuclear zinc active site important for melanogenesis, Angew. Chem. Int. Ed. 56 (33) (2017) 9812–9815.
[4] V. Del Marmol, S. Ito, I. Jackson, J. Vachtenheim, P. Berr, G. Ghanem, R. Morandini, K. Wakamatsu, G. Huez, TRP-1 expression correlates with eumelanogenesis in human pigment cells in culture, FEBS Lett. 327 (3) (1993) 307–310.
[5] Á. Sánchez-Ferrer, J.N. Rodríguez-López, F. García-Cánovas, F. García-Carmona, Tyrosinase: a comprehensive review of its mechanism, Biochim. Biophys. Acta Protein Struct. Mol. Enzymol. 1247 (1) (1995) 1–11.
[6] O. Nerya, R. Musa, S. Khatib, S. Tamir, J. Vaya, Chalcones as potent tyrosinase inhibitors: the effect of hydroxyl positions and numbers, Phytochemistry 65 (10) (2004) 1389–1395.
[7] S. Piña-Oviedo, C. Ortiz-Hidalgo, A.G. Ayala, Human colors—the rainbow garden of pathology: what gives normal and pathologic tissues their color? Arch. Pathol. Lab Med. 141 (3) (2017) 445–462.
[8] J.L. Rees, Genetics of hair and skin color, Annu. Rev. Genet. 37 (1) (2003) 67–90.
[9] S. Del Bino, C. Duval, F. Bernerd, Clinical and biological characterization of skin pigmentation diversity and its consequences on UV impact, Int. J. Mol. Sci. 19 (9) (2018) 2668.
[10] F. Solano, On the metal cofactor in the tyrosinase family, Int. J. Mol. Sci. 19 (2) (2018) 633.
[11] M. Ashooriha, M. Khoshneviszadeh, M. Khoshneviszadeh, S.E. Moradi, A. Rafiei, M. Kardan, S. Emami, 1, 2, 3-Triazole-based kojic acid analogs as potent tyrosinase inhibitors: design, synthesis and biological evaluation, Bioorg. Chem. 82 (2019) 414–422.
[12] K. Zborowski, R. Gryboś, L.M. Proniewicz, Determination of the most stable structures of selected hydroxypyrones and their cations and anions, J. Mol. Struct.: THEOCHEM 639 (1–3) (2003) 87–100.
[13] S. Grabowsky, T. Pfeuffer, W. Morgenroth, C. Paulmann, T. Schirmeister, P. Luger, A comparative study on the experimentally derived electron densities of three protease inhibitor model compounds, Org. Biomol. Chem. 6 (13) (2008) 2295–2307.
[14] S. Grabowsky, T. Pfeuffer, L. Chęcińska, M. Weber, W. Morgenroth, P. Luger, T. Schirmeister, Electron-density determination of electrophilic building blocks as model compounds for protease inhibitors, European journal of organic chemistry 2007 17 (2007) 2759–2768.

[15] N. Bouhmaida, F. Bonhomme, B. Guillot, C. Jelsch, N.E. Ghermani, Charge density and electrostatic potential analyses in paracetamol, Acta Crystallogr. Sect. B Struct. Sci. 65 (3) (2009) 363–374.
[16] E.J. Yearley, E.A. Zhurova, V.V. Zhurov, A.A. Pinkerton, Binding of genistein to the estrogen receptor based on an experimental electron density study, J. Am. Chem. Soc. 129 (48) (2007) 15013–15021.
[17] E.A. Zhurova, C.F. Matta, N. Wu, V.V. Zhurov, A.A. Pinkerton, Experimental and theoretical electron density study of estrone, J. Am. Chem. Soc. 128 (27) (2006) 8849–8861.
[18] C. Matta, Challenges and Advances in Computational Chemistry and Physics Series, Springer, 2006.
[19] E.A. Zhurova, V.V. Zhurov, D. Chopra, A.I. Stash, A.A. Pinkerton, 17α-Estradiol· 1/2 H2O: super-structural ordering, electronic properties, chemical bonding, and biological activity in comparison with other estrogens, J. Am. Chem. Soc. 131 (47) (2009) 17260–17269.
[20] D.S. Arputharaj, V.R. Hathwar, T.N. Guru Row, P. Kumaradhas, Topological electron density analysis and electrostatic properties of aspirin: an experimental and theoretical study, Cryst. Growth Des. 12 (9) (2012) 4357–4366.
[21] G. Rajalakshmi, V.R. Hathwar, P. Kumaradhas, Intermolecular interactions, charge-density distribution and the electrostatic properties of pyrazinamide anti-TB drug molecule: an experimental and theoretical charge-density study, Acta Crystallogr. B: Structural Science, Crystal Engineering and Materials 70 (3) (2014) 568–579.
[22] G. Rajalakshmi, V.R. Hathwar, P. Kumaradhas, Topological analysis of electron density and the electrostatic properties of isoniazid: an experimental and theoretical study, Acta Crystallogr. B: Structural Science, Crystal Engineering and Materials 70 (2) (2014) 331–341.
[23] E.A. Zhurova, V.V. Zhurov, P. Kumaradhas, S. Cenedese, A.A. Pinkerton, Charge density and electrostatic potential study of 16α, 17β-estriol and the binding of estrogen molecules to the estrogen receptors ERα and ERβ, J. Phys. Chem. B 120 (34) (2016) 8882–8891.
[24] C. Kalaiarasi, M.S. Pavan, P. Kumaradhas, Topological characterization of electron density, electrostatic potential and intermolecular interactions of 2-nitroimidazole: an experimental and theoretical study, Acta Crystallogr. B: Structural Science, Crystal Engineering and Materials 72 (5) (2016) 775–786.
[25] S. Manjula, C. Kalaiarasi, M.S. Pavan, V.R. Hathwar, P. Kumaradhas, Charge density and electrostatic potential of hepatitis C anti-viral agent andrographolide: an experimental and theoretical study, Acta Crystallogr. B: Structural Science, Crystal Engineering and Materials 74 (6) (2018).
[26] A. Hasil, A. Mehmood, M. Ahmed, Experimental and theoretical charge-density analysis of hippuric acid: insight into its binding with human serum albumin, Acta Crystallogr. B: Structural Science, Crystal Engineering and Materials 75 (4) (2019).
[27] N. Muzet, B. Guillot, C. Jelsch, E. Howard, C. Lecomte, Electrostatic complementarity in an aldose reductase complex from ultra-high-resolution crystallography and first-principles calculations, Proc. Natl. Acad. Sci. Unit. States Am. 100 (15) (2003) 8742–8747.
[28] S. Bruker, S. Saint, Bruker AXS Inc, Madison, Wisconsin, USA, 2002.
[29] L. Krause, R. Herbst-Irmer, G.M. Sheldrick, D. Stalke, Comparison of silver and molybdenum microfocus X-ray sources for single-crystal structure determination, J. Appl. Crystallogr. 48 (1) (2015) 3–10.
[30] O.V. Dolomanov, L.J. Bourhis, R.J. Gildea, J.A. Howard, H. Puschmann, OLEX2: a complete structure solution, refinement and analysis program, J. Appl. Crystallogr. 42 (2) (2009) 339–341.
[31] F.H. Allen, I.J. Bruno, Bond lengths in organic and metal-organic compounds revisited: X—H bond lengths from neutron diffraction data, Acta Crystallogr. Sect. B Struct. Sci. 66 (3) (2010) 380–386.
[33] M.N. Burnett, C.K. Johnson, Orteps, Oak Ridge Thermal Ellipsoid Plot Program for Crystal Structure Illustrations, Oak Ridge National Laboratory Report ORNL-6895, 1996. Tennessee.
[34] C. Jelsch, B. Guillot, A. Lagoutte, C. Lecomte, Advances in protein and small-molecule charge-density refinement methods using MoPro, J. Appl. Crystallogr. 38 (1) (2005) 38–54.
[35] A.Ø. Madsen, SHADE web server for estimation of hydrogen anisotropic displacement parameters, J. Appl. Crystallogr. 39 (5) (2006) 757–758.
[36] E. Clementi, C. Roetti, Roothaan-Hartree-Fock atomic wavefunctions: basis functions and their coefficients for ground and certain excited states of neutral and ionized atoms, Z≤ 54, Atomic Data Nucl. Data Tables 14 (3–4) (1974) 177–478.
[37] N.K. Hansen, P. Coppens, Testing aspherical atom refinements on small-molecule data sets, Acta Crystallogr. Sect. A Cryst. Phys. Diffr. Theor. Gen. Crystallogr. 34 (6) (1978) 909–921.
[38] V.V. Zhurov, E.A. Zhurova, A.A. Pinkerton, Optimization and evaluation of data quality for charge density studies, J. Appl. Crystallogr. 41 (2) (2008) 340–349.
[39] P. Giannozzi, O. Andreussi, T. Brumme, O. Bunau, M.B. Nardelli, M. Calandra, R. Car, C. Cavazzoni, D. Ceresoli, M. Cococcioni, Advanced capabilities for materials modelling with Quantum ESPRESSO, J. Phys. Condens. Matter 29 (46) (2017) 465901.
[40] J.P. Perdew, K. Burke, M. Ernzerhof, Generalized gradient approximation made simple, Phys. Rev. Lett. 77 (18) (1996) 3865.
[41] S. Grimme, J. Antony, S. Ehrlich, H. Krieg, A consistent and accurate ab initio parametrization of density functional dispersion correction (DFT-D) for the 94 elements H-Pu, J. Chem. Phys. 132 (15) (2010) 154104.
[42] P.E. Blöchl, Projector augmented-wave method, Phys. Rev. B 50 (24) (1994) 17953.
[43] M. Ahmed, C. Jelsch, B. Guillot, C. Lecomte, S. Domagała, Relationship between stereochemistry and charge density in hydrogen bonds with oxygen acceptors, Cryst. Growth Des. 13 (1) (2012) 315–325.
[44] S.G. Aziz, A.O. Alyoubi, S.A. Elroby, R.H. Hilal, Electronic structure and acid–base properties of Kojic acid and its dimers. A DFT and quantum topology study, Mol. Phys. 115 (20) (2017) 2565–2576.
[45] A. Halasa, I. Reva, L. Lapinski, H. Rostkowska, R. Fausto, M.J. Nowak, Conformers of kojic acid and their near-IR-induced conversions: long-range intramolecular vibrational energy transfer, J. Phys. Chem. 120 (17) (2016) 2647–2656.
[46] M. Turner, J. McKinnon, S. Wolff, D. Grimwood, P. Spackman, D. Jayatilaka, M. Spackman, CrystalExplorer17, University of Western Australia Crawley, Western Australia, Australia, 2017.
[47] A.D. Martin, J. Britton, T.L. Easun, A.J. Blake, W. Lewis, M. Schröder, Hirshfeld surface investigation of structure-directing interactions within dipicolinic acid derivatives, Cryst. Growth Des. 15 (4) (2015) 1697–1706.
[48] R. Bader, Quantum topology of molecular charge distributions. III. The mechanics of an atom in a molecule, J. Chem. Phys. 73 (6) (1980) 2871–2883.
[49] R.J. Gillespie, P.L. Popelier, Chemical Bonding and Molecular Geometry, Oxford University Press, 2001.
[50] D. Stalke, Meaningful structural descriptors from charge density, Chemistry–A European Journal 17 (34) (2011) 9264–9278.
[51] R. Kakkar, C. Singh, Theoretical study of the kojic acid structure in gas phase and aqueous solution, Int. J. Quant. Chem. 111 (15) (2011) 4318–4329.
[52] K. Hryniewicz, K. Stadnicka, A. Pattek-Janczyk, Crystal structure and vibrational spectra of 2-chloromethyl-5-hydroxy-4H-pyran-4-one and 5-hydroxy-2-methyl-4H-pyran-4-one as potential ligands for Fe (III) complexes, J. Mol. Struct. 919 (1–3) (2009) 255–270.
[53] A. Krawczuk, K. Stadnicka, Experimental and theoretical charge density study of the chemical bonding in chlorokojic acid crystal structure, J. Phys. Chem. 116 (39) (2012) 9759–9768.
[54] M. Uher, V. Konecny, O. Rajniakova, Synthesis of 5-hydroxy-2-hydroxymethyl-4H-pyran-4-one derivatives with pesticide activity, Chem. Pap. 48 (4) (1994) 282.
[55] R. Bader, A Quantum Theory, Clarendon, Oxford, UK, 1990.
[56] R.F. Bader, A bond path: a universal indicator of bonded interactions, J. Phys. Chem. 102 (37) (1998) 7314–7323.
[57] C. Gatti, Chemical bonding in crystals: new directions, Z. für Kristallogr. - Cryst. Mater. 220 (5/6) (2005) 399–457.
[58] S.J. Grabowski, Hydrogen Bonding: New Insights, Springer, 2006.
[59] P. Gilli, V. Bertolasi, V. Ferretti, G. Gilli, Covalent nature of the strong homonuclear hydrogen-bond-Study of the OH—O system by crystal-structure correlation methods, J. Am. Chem. Soc. 116 (3) (1994) 909–915.
[60] E. Espinosa, E. Molins, Retrieving interaction potentials from the topology of the electron density distribution: the case of hydrogen bonds, J. Chem. Phys. 113 (14) (2000) 5686–5694.
[61] E. Espinosa, I. Alkorta, J. Elguero, E. Molins, From weak to strong interactions: a comprehensive analysis of the topological and energetic properties of the electron density distribution involving X–H··· F–Y systems, J. Chem. Phys. 117 (12) (2002) 5529–5542.
[62] C.F. Matta, Hydrogen–Hydrogen Bonding: the Non-electrostatic Limit of Closed-Shell Interaction between Two Hydro, Hydrogen Bonding—New Insights, Springer, 2006, pp. 337–375.
[63] C.F. Matta, J. Hernández-Trujillo, T.H. Tang, R.F. Bader, Hydrogen–hydrogen bonding: a stabilizing interaction in molecules and crystals, Chemistry–A European Journal 9 (9) (2003) 1940–1951.
[64] M. Sendovski, M. Kanteev, V. Shuster, N. Adir, A. Fisherman, Crystal structure of tyrosinase from Bacillus magaterium in complex with inhibitor kojic acid, J. Mol. Biol. 405 (2011) 227–237.
[65] R.F. Bader, Atoms in molecules, Acc. Chem. Res. 18 (1) (1985) 9–15.
[66] A.I. Stash, V.G. Tsirelson, Developing WinXPRO: a software for determination of the multipole-model-based properties of crystals, J. Appl. Crystallogr. 47 (6) (2014) 2086–2089.
[67] P. Kumar, P.M. Dominiak, Structural and dynamical aspects of electrostatic interactions by applying aspherical atom model in HIV-1 protease, Biophys. J. 110 (3) (2016) 380a.
[68] G. Rajalakshmi, M.S. Pavan, P. Kumaradhas, Charge density distribution and electrostatic interactions of ethionamide: an inhibitor of the enoyl acyl carrier protein reductase (inhA) enzyme of Mycobacterium tuberculosis, RSC Adv. 4 (101) (2014) 57823–57833.
[69] B. Fournier, E.-E. Bendeif, B. Guillot, A. Podjarny, C. Lecomte, C. Jelsch, Charge density and electrostatic interactions of fidarestat, an inhibitor of human aldose reductase, J. Am. Chem. Soc. 131 (31) (2009) 10929–10941.
[70] P.M. Dominiak, A. Volkov, X. Li, M. Messerschmidt, P. Coppens, A theoretical databank of transferable aspherical atoms and its application to electrostatic interaction energy calculations of macromolecules, J. Chem. Theor. Comput. 3 (1) (2007) 232–247.
[71] P. Politzer, J.S. Murray, The fundamental nature and role of the electrostatic potential in atoms and molecules, Theoretical Chemistry Accounts 108 (3) (2002) 134–142.
[72] Z. Su, P. Coppens, On the mapping of electrostatic properties from the multipole description of the charge density, Acta Crystallogr. A: Foundations of Crystallography 48 (2) (1992) 188–197.
[73] U. Koch, P.L.A. Popelier, Characterization of C—H—0 hydrogen bonds on the basis of the charge DensityJ, Phys. Chem. 99 (1995) 9747–9754.